Check for updates

Li-CO_2 Batteries Hot Paper

How to cite: *Angew. Chem. Int. Ed.* **2022,** *61,* e202114612
International Edition: doi.org/10.1002/anie.202114612
German Edition: doi.org/10.1002/ange.202114612

High-Efficiency and Stable Li–CO_2 Battery Enabled by Carbon Nanotube/Carbon Nitride Heterostructured Photocathode

Jiaxin Li, Kun Zhang, Yang Zhao, Chuang Wang, Lipeng Wang, Lie Wang, Meng Liao, Lei Ye, Ye Zhang, Yue Gao, Bingjie Wang, and Huisheng Peng**

Abstract: *Li–CO_2 batteries are explored as promising power systems to alleviate environmental issues and to implement space applications. However, sluggish cathode kinetics of CO_2 reduction/evolution result in low round-trip efficiency and poor cycling stability of the fabricated energy-storage devices. Herein, we design a heterostructued photocathode comprising carbon nanotube and carbon nitride to accelerate cathode reactions of a Li–CO_2 battery under illumination. Benefiting from the unique defective structure of carbon nitride and favorable interfacial charge transfer, the photocathode effectively harvests ultraviolet-visible light to generate abundant photoexcited carriers and coordinates energetic photoelectrons/holes to participate in the discharge/charge reactions, leading to efficient photo-energy utilization in decreasing reaction barriers and enhancing thermodynamic reversibility of Li–CO_2 battery. The resulting battery delivers a high round-trip efficiency of 98.8 % (ultralow voltage hysteresis of 0.04 V) and superior cycling stability (86.1 % efficiency retention after 100 cycles).*

Lithium–carbon dioxide (Li–CO_2) battery technology is highly valuable for addressing global warming and fossil fuel crisis simultaneously because it can fix CO_2 and store energy in a simple device ($4Li + 3CO_2 \rightleftharpoons 2Li_2CO_3 + C$, $E^0 = 2.80$ V).[1] Besides, it shows significant application perspectives on Mars with ultrahigh CO_2 concentration in the atmosphere.[2] However, owing to serious kinetic barriers between CO_2 and discharge products (Li_2CO_3 and C), the promising technology remains at a conceptional stage with large voltage hysteresis (the sum of charge and discharge overpotentials) of above 1.0 V, low round-trip efficiencies (the ratio of energy output during discharge to energy input during charge) of below 70 %, and limited areal capacities of below 5 mAh cm^{-2} (Table S1).[3] High polarized voltages also trigger various side reactions associated with electrolyte and carbon-based cathode, further aggravating cycling stability of the battery.[4] Therefore, optimized cathode designs have been constantly sought to achieve efficient and stable Li–CO_2 batteries.[5]

Utilizing light to drive slow electrode reactions represents a promising strategy to decrease overpotentials and raise round-trip efficiencies of metal–air batteries, which is achieved by integrating photocatalysts into air cathodes.[6] When the photons of suitable energy are harvested by photocatalysts, electrons are excited to the conduction band (CB) from the valence band (VB), along with the generation of numerous electron-hole pairs. These active photoexcited carriers are expected to overcome serious kinetic barriers of gas reduction/evolution reactions and achieve conversion/storage of photo-energy in the battery. However, poor visible-light absorption (accounting for about 40 % of the solar spectrum) and severe carrier recombination of semiconductor photocatalysts seriously hinder effective photo-energy utilization in the target cathode reactions and compromise achievable electrochemical performances of Li–CO_2 batteries.[6d,7] For example, the reported high-efficiency light-involved Li–CO_2 batteries are typically achieved at low cut-off capacity (e.g., 0.01 mAh cm^{-2}) and current density (e.g., 0.01 mA cm^{-2}), while their cycling stability is also unsatisfactory.[8] This necessitates a well-designed photocathode that can effectively utilize photo-energy to boost sluggish CO_2 reduction/evolution reactions.

Herein, we design an interwoven CNT conductive scaffold coated by a carbon nitride layer with nitrogen defects (CNT@C_3N_4) as a heterostructured photocathode operated in a quasi-solid Li–CO_2 battery to solve the above problems. The defective C_3N_4 enables efficient ultraviolet-visible light absorption to produce abundant photoelectrons/holes, and the favorable charge transfer between C_3N_4 and CNT ensures that more photoelectrons/holes migrate to drive CO_2 reduction/evolution reactions instead of recombination (Figure 1). The increased generation and inhibited recombination of charge carriers result in efficient photo-energy utilization in boosting the sluggish cathode kinetics. Consequently, CO_2 molecules are reduced to Li_2CO_3/C by

[*] J. Li, K. Zhang, C. Wang, L. Wang, M. Liao, L. Ye, Prof. Y. Gao, Prof. B. Wang, Prof. H. Peng
State Key Laboratory of Molecular Engineering of Polymers, Department of Macromolecular Science, and Laboratory of Advanced Materials, Fudan University
Shanghai 200438 (P. R. China)
E-mail: wangbingjie@fudan.edu.cn
penghs@fudan.edu.cn

Prof. Y. Zhao
Frontiers Science Center for Flexible Electronics
Institute of Flexible Electronics
Northwestern Polytechnical University
Xi'an 710072 (P. R. China)

Dr. L. Wang, Prof. Y. Zhang
National Laboratory of Solid-State Microstructures
Jiangsu Key Laboratory of Artificial Functional Materials
Chemistry and Biomedicine Innovation Center (ChemBIC)
Collaborative Innovation, Center of Advanced Microstructures
College of Engineering and Applied Sciences
Nanjing University
Nanjing 210023 (P. R. China)

© 2021 Wiley-VCH GmbH

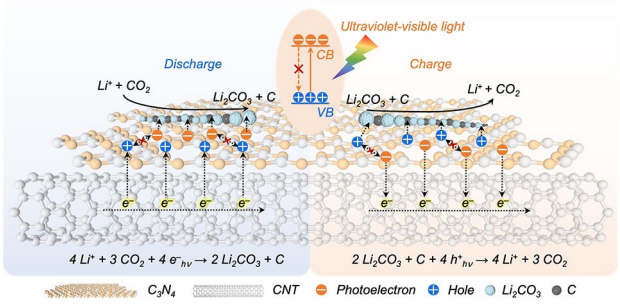

Figure 1. Depiction of the light-assisted discharge/charge processes at the CNT@C_3N_4 heterostructured photocathode. The heterostructured photocathode captures the ultraviolet-visible light and generates numerous active photoelectrons and holes. Benefiting from the favorable interfacial charge transfer, photoelectrons move to reduce CO_2 to Li_2CO_3/C during discharge, while holes migrate to decompose discharge products to CO_2 during charge. Extended visible-light absorption and enhanced carrier separation/transfer contribute together to the light-promoted cathode reactions under illumination.

photoelectrons at 3.24 V, exceeding the thermodynamic equilibrium voltage (2.80 V vs. Li^+/Li); the products are oxidized to CO_2/Li^+ by holes at 3.28 V in the subsequent charging process. The assembled Li–CO_2 batteries achieve an ultrahigh round-trip efficiency of 98.8 % (ultralow voltage hysteresis of 0.04 V) and robust cycling stability (86.1 % efficiency retention after 100 cycles), much exceeding the existing Li–CO_2 batteries. Furthermore, the implementation of the photocathode allows for the construction of a flexible Li–CO_2 fiber battery, demonstrating potentials for wearable applications.

The CNT@C_3N_4 heterostructured photocathode was prepared by in situ synthesis of a C_3N_4 thin-layer on a free-standing hydrophilic CNT film (Figure S1). The hydrophilic pretreatment ensured the effective contact between CNT and aqueous precursor solution, and enabled the uniform coating of C_3N_4 on the CNT surface instead of forming random aggregates among CNT bundles, which was vital to the construction of a heterostructured photocathode with desirable performances (Figure S2). Importantly, the heterostructured cathode was prepared at a higher temperature of 600 °C than typical 550 °C in this study. Higher condensation temperature induced the loss of ordered structure and the generation of nitrogen defects within C_3N_4 (Figure S3). This further caused the redshift of the absorption edge and the enhancement of carrier separation efficiency in C_3N_4 (Figure S4),[9] which would facilitate the photo-energy utilization for CO_2 reduction/evolution reactions. Similar to the pristine CNT, the as-prepared CNT@C_3N_4 presented an interconnected network structure comprising abundant micrometer-sized pores (Figures 2a–d and S5). The interwoven conductive scaffold structure favored CO_2/ion diffusion and solid product storage, and the abundant heterointerfaces enabled fast separation/transfer of photoexcited carriers. The uniform distributions of N and C elements over the whole CNT@C_3N_4 film were confirmed in Figure S6. The characteristic absorption peaks assigned to C_3N_4 were observed in the infrared spectrum of CNT@C_3N_4,[10] indicating the successful deposition of C_3N_4 on the CNT film

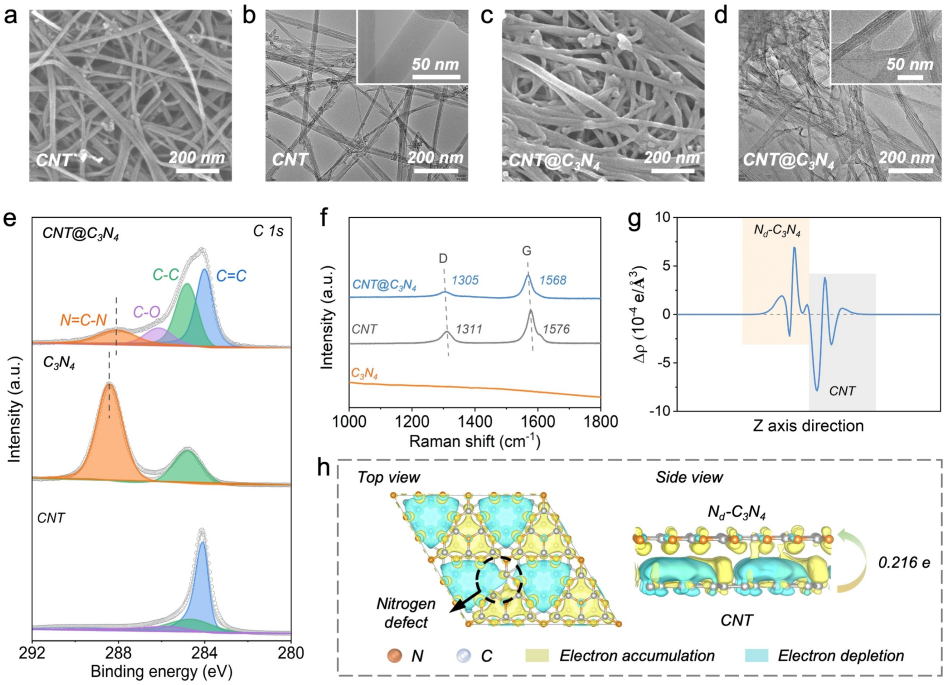

Figure 2. Structural characterizations of CNT@C_3N_4 heterostructured photocathode. a–d) Scanning electron microscopy and transmission electron microscopy images of (a, b) CNT and (c, d) CNT@C_3N_4. e) C 1s X-ray photoelectron spectra and f) Raman spectra of CNT, C_3N_4, and CNT@C_3N_4. g) Planar-averaged electron density difference Δρ of CNT/defective C_3N_4 (N_d-C_3N_4) heterojunction. Average electrostatic potential profiles along the Z-axis direction of CNT and N_d-C_3N_4. h) Top and side views of three-dimensional charge density difference plots of CNT and N_d-C_3N_4.

© 2021 Wiley-VCH GmbH

15213773, 2022, 4, Downloaded from https://onlinelibrary.wiley.com/doi/10.1002/anie.202114612 by Fudan University, Wiley Online Library on [12/12/2024]. See the Terms and Conditions (https://onlinelibrary.wiley.com/terms-and-conditions) on Wiley Online Library for rules of use; OA articles are governed by the applicable Creative Commons License

(Figure S7). In the C 1s X-ray photoelectron spectra, the N–C=N peak shifted from 288.4 eV of C_3N_4 to 288.1 eV of CNT@C_3N_4 (Figure 2e), implying increased electron density of C atoms in the N–C=N units of CNT@C_3N_4.[11] A similar shift in the N 1s X-ray photoelectron spectra also supported the electron transfer from CNT to C_3N_4 (Figure S8). Besides, the shifts of D and G bands, as well as the restrained photoluminescence effect shown in the Raman spectra of CNT@C_3N_4, also verified the electronic coupling effect (Figure 2f).[12] In comparison, the physical mixture of CNT and C_3N_4 presented strong fluorescence signals similar to the bare C_3N_4 because of the unfavorable interfacial contact between the two materials (Figure S9).

Density functional theory calculations were further carried out to investigate the electronic behavior at the heterostructure. The above morphologic and structural characterizations of CNT@C_3N_4 showed that C_3N_4 was uniformly coated on CNT surfaces with abundant interfaces and effective contact between them. To this end, the CNT@C_3N_4 heterostructure was modeled as a stable bilayer parallel stacking configuration consisting of a defective C_3N_4 monolayer (N_d-C_3N_4, 2×2 C_3N_4 supercell with a removed pyridine N atom) and a graphene monolayer to provide fundamental understandings of the heterostructure interactions.[13] First, the adhesion energy was calculated as −0.36 eV for the entire interface model, proving the high structural stability of the heterostructure and the strong electronic interaction between CNT and N_d-C_3N_4. Then, the planar-averaged electron density difference plot revealed that the N_d-C_3N_4 part was negatively charged while the CNT part was positively charged near the interface, implying the electron transferred from CNT to N_d-C_3N_4 (Figure 2g). The electrons would spontaneously redistribute at the heterostructure, leading to the electron-rich regions under the triazine units and the electron-depletion regions at the nanopores of N_d-C_3N_4 (Figure 2h). Importantly, there were van der Waals interactions between the conjugated triazine ring motifs of N_d-C_3N_4 and the graphene fragments of CNT, accounting for the enhanced charge separation/transfer. Overall, 0.216*e* transferred from the CNT to N_d-C_3N_4 in the specified model. The charge transfer direction was in agreement with the results of X-ray photoelectron spectra (Figure 2e). Therefore, both the experimental and theoretical results have proved the electronic coupling effect at the CNT@C_3N_4 heterostructure.

The light-harvesting ability, carrier separation efficiency, and band structure of the heterostructured photocathode were further analyzed. First, CNT@C_3N_4 presented an absorption range from ultraviolet to visible light attributed to superior light capture abilities of C_3N_4 and CNT (Figure 3a). Further, CNT@C_3N_4 exhibited much weaker fluorescence intensity than bare C_3N_4, proving enhanced separation and transfer efficiency of photogenerated carriers at the heterostructure (Figure 3b). This was also supported by the stronger response photocurrent, prolonged fluorescent lifetime, and lower resistance of CNT@C_3N_4 than C_3N_4 (Figures 3c and S10). Besides, finite difference time domain simulations showed that the electric near-field amplitude could be enhanced around CNT@C_3N_4 under different

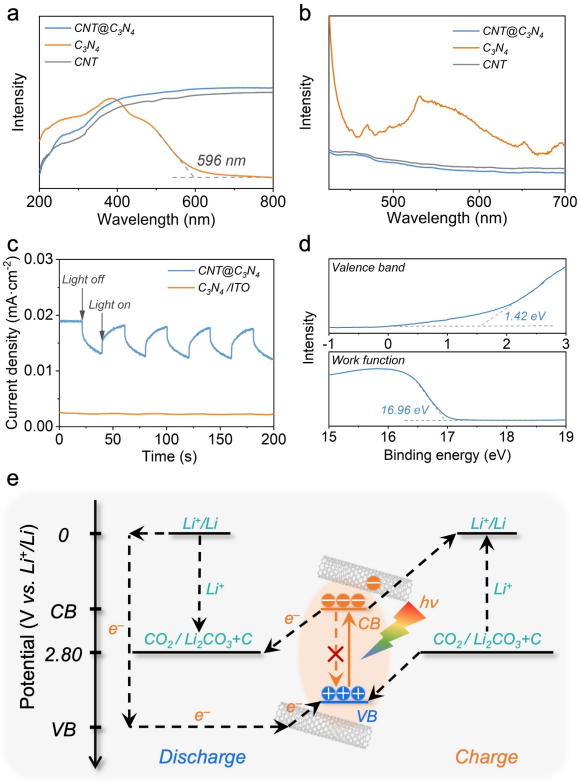

Figure 3. Optical properties, photoelectrochemical performance, and band structure of CNT@C_3N_4 heterostructured photocathode. a) Diffuse reflectance ultraviolet-visible absorption spectra and b) steady-state photoluminescence spectra of CNT, C_3N_4, and CNT@C_3N_4. c) Periodic on/off photocurrent responses of CNT@C_3N_4 and C_3N_4 coated on the indium tin oxide (ITO). d) Ultraviolet photoelectron spectra of C_3N_4. e) Proposed working mechanism of the light-assisted Li–CO_2 battery based on the CNT@C_3N_4 heterostructured photocathode.

wavelengths, which would also contribute to more carrier generation and higher catalytic efficiency (Figure S11).[14] Combining the ultraviolet photoelectron spectroscopy and Tauc curves, the CB and VB edges of CNT@C_3N_4 were calculated as 1.84 and 4.41 V vs. Li^+/Li (Figures 3d and S12). Since the CB potential was below the reduction potential between CO_2 and Li_2CO_3/C (2.80 V vs. Li^+/Li), the photoelectrons could participate in the discharge reactions of Li–CO_2 battery. In a reverse charging process, the holes could boost the charge reactions of Li–CO_2 battery because the VB potential was above the oxidation potential between Li_2CO_3/C and CO_2 (2.80 V vs. Li^+/Li). As a supplement, CNT@C_3N_4 showed higher activity for CO_2 reduction/evolution reactions than bare CNT (Figure S13), confirming the contribution of photocatalytic process to the accelerated cathode reactions. The above results indicated that the CNT@C_3N_4 heterostructured photocathode guaranteed the efficient generation, separation, transfer, and utilization of photogenerated carriers in the target battery processes.

The working mechanism of a light-assisted Li–CO_2 battery based on the CNT@C_3N_4 heterostructured photocathode is illustrated in Figure 3e. C_3N_4 firstly harvests

© 2021 Wiley-VCH GmbH

15213773, 2022, 4, Downloaded from https://onlinelibrary.wiley.com/doi/10.1002/anie.202114612 by Fudan University, Wiley Online Library on [12/12/2024]. See the Terms and Conditions (https://onlinelibrary.wiley.com/terms-and-conditions) on Wiley Online Library for rules of use; OA articles are governed by the applicable Creative Commons License

photons with matching energy and produces numerous photoelectrons and holes under illumination. During discharge, photoelectrons with strong reductive activity rapidly migrate to the photocathode surface and reduce CO_2 to $C_2O_4^{2-}$ via a one-electron pathway and the adsorbed $C_2O_4^{2-}$ further disproportionate into the final discharge products after several reaction steps ($CO_2 + e^- \rightarrow 1/2C_2O_4^{2-}$, $C_2O_4^{2-} \rightarrow CO_2^{2-} + CO_2$, $C_2O_4^{2-} + CO_2^{2-} \rightarrow 2CO_3^{2-} + C$, $CO_3^{2-} + 2Li^+ \rightarrow Li_2CO_3$). Meanwhile, the photogenerated holes are rapidly neutralized with the electrons from the external circuit instead of recombining with photoelectrons benefiting from the fast interfacial charge-transfer. During charge, holes oxidize discharge products to CO_2/Li^+ at an applied voltage, while photoelectrons quickly transfer from C_3N_4 to CNT and further migrate to reduce Li^+ to Li at the anode via the external circuit. The theoretical discharge and charge voltages of the light-assisted Li–CO_2 battery is determined by the VB and CB potentials of the photocatalyst (4.41 and 1.84 V vs. Li^+/Li), respectively. Importantly, the theoretical discharge voltage has surpassed the equilibrium potential of product formation (2.80 V vs. Li^+/Li), indicating the conversion of photo-energy to electric energy during discharge. The participation of holes reduces the inputting of electric energy during charge and achieves the storage of photo-energy in the battery.

The light-assisted Li–CO_2 battery was assembled with a CNT@C_3N_4 heterostructured photocathode, a lithium anode, and a quasi-solid gel electrolyte (Figure S14). A 350 W Xenon lamp with a wavelength distribution from 380 to 780 nm and a power density of about 110 mW cm^{-2} was used as light source (Figure S15). Notably, the electrolyte exhibited good mechanical toughness, high ionic conductivity, decent electrochemical stability, and thermal stability, showing huge potentials in flexible batteries (Figure S16). After battery assembly, the morphology and structure of the cathodes during discharge/charge were first analyzed to confirm the thermodynamic rationality of the Li–CO_2 battery in the light and dark. The similar spherical particles were deposited on the interior and surface of porous cathodes after discharge, but the products in the dark ($\approx$200 nm in size) were much larger than the light-mediated products ($\approx$70 nm in size) (Figures 4a, b). These particle-shaped products are typically considered to be generated via a solution-based pathway and are favored for realizing higher capacity because they avoid the charge-transfer limitations of insulating products.[15] The similar particle-shaped morphologies suggested that the discharge products were prone to be produced via a solution pathway instead of a surface pathway whether in the light or dark.[16] But the abundant photoelectrons provided more nucleation sites and induced more small particles in the light (Figure S17). The small particles are generally believed to be easily degradable due to their short charge transfer pathways and large surface areas.[17] Figures 4c and d showed these particles could be fully decomposed without apparent residuals after recharging under illumination, in contrast with the undecomposed fragments piling up at the cathode in the dark. Besides the important role of holes in the

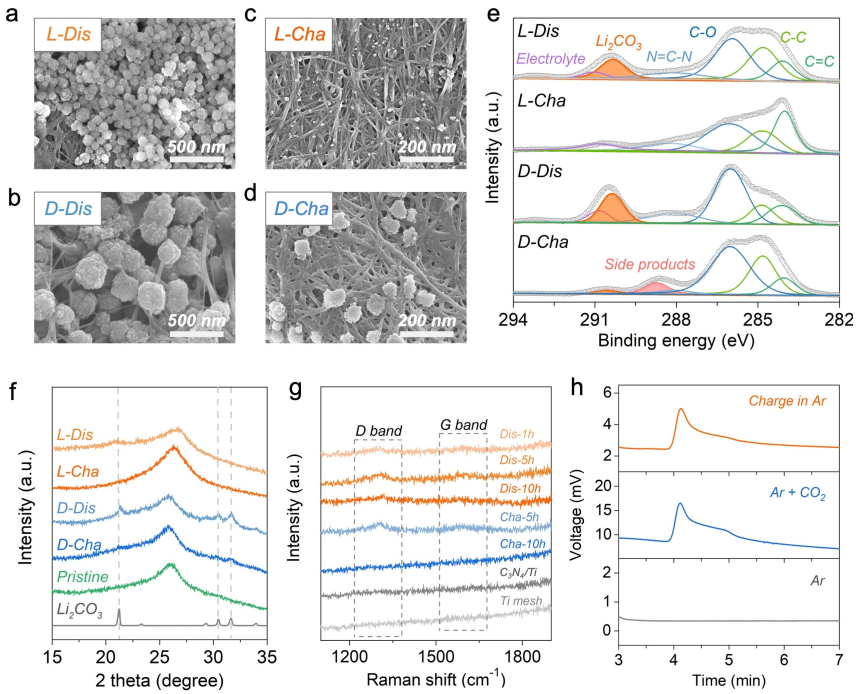

Figure 4. Thermodynamic feasibility analysis of light-assisted Li–CO_2 batteries. a–d) Scanning electron microscopy images, e) C 1s X-ray photoelectron spectra, and f) X-ray diffraction patterns of the heterostructured photocathodes collected from Li–CO_2 batteries at corresponding discharge/charge states. *L-Dis*, *L-Cha*, *D-Dis*, and *D-Cha* represent the batteries discharged or recharged in light or dark conditions. g) Raman spectra of the carbon-free C_3N_4/Ti mesh cathodes collected from Li–CO_2 batteries at corresponding discharge/charge states. h) Gas chromatography signal plots of pure Ar, the mixture gas of Ar and CO_2, and the gas products from the Li–CO_2 battery during charge in Ar.

© 2021 Wiley-VCH GmbH

15213773, 2022, 4, Downloaded from https://onlinelibrary.wiley.com/doi/10.1002/anie.202114612 by Fudan University, Wiley Online Library on [12/12/2024]. See the Terms and Conditions (https://onlinelibrary.wiley.com/terms-and-conditions) on Wiley Online Library for rules of use; OA articles are governed by the applicable Creative Commons License

enhanced battery rechargeability, the light-mediated product morphology also contributed to the lowered charging voltages.

Further, both the X-ray photoelectron spectra and infrared spectra proved that discharge product Li_2CO_3 was generated and fully decomposed under illumination (Figures 4e and S18). After discharging in the dark, the discharge product Li_2CO_3 was observed while no obvious by-products were detected at the cathode surface. However, the decomposition of products in the dark was accompanied by the formation of by-products, probably derived from the electrolyte decomposition and cathode corrosion.[18] X-ray diffraction spectroscopy also confirmed these particles produced in the dark as Li_2CO_3 according to the characteristic peaks of 21.2°, 30.5°, and 31.5°; the weakened but remained signals indicated that these product particles underwent incomplete degradations during charge (Figure 4f). Especially, no sharp diffraction peaks of Li_2CO_3 appeared in the pattern of the discharged cathode under illumination, probably owing to the terrible crystallinity of light-mediated products.[19] In the meantime, the formation/decomposition of carbon during discharge/charge was also verified at a carbon-free C_3N_4/Ti mesh cathode under illumination, according to the increased/decreased intensities of D and G bands related to the carbon species in Raman spectra (Figure 4g). The CO_2 evolution during charge was confirmed by gas chromatography (Figure 4h), supporting the thermodynamic feasibility of the charging process. Besides, the stability of electrolytes in the light and dark was evaluated by the ^1H and ^{13}C nuclear magnetic resonance spectroscopy (Figure S19). The position and intensity of the peaks corresponding to the major electrolyte components and H_2O/HDO did not change significantly after cycling in the light indicating the stability of the electrolyte in the light, attributed to the lowered polarized voltages. In comparison, the ionic liquid partly decomposed to N-heterocyclic carbene molecules after cycling under the excessive overpotentials in the dark.

After confirming the thermodynamic feasibility of the Li–CO_2 battery, the electrochemical properties were then systematically evaluated. The instantly decreased overpotentials under the applied light indicated the sensitive light-responsiveness of the heterostructured photocathode (Figure S20), which could also be confirmed by the instantly lowered resistance and increased response current under illumination (Figure S21). With current densities increasing from 0.02 to 0.40 mA cm^{-2} (areal capacity increasing from 0.02 to 0.40 mAh cm^{-2}), the discharge voltages decreased from 3.24 to 2.73 V and the charge voltages increased from 3.28 to 3.96 V (Figure S22), indicating the feasibility of high-current-density and high-specific-capacity operation. Notably, at 0.02 mA cm^{-2}, the discharge/charge voltage of 3.24/3.28 V at the first cycle corresponded to an ultralow polarized voltage gap of 0.04 V and a record-high round-trip efficiency of 98.8 % (Figure 5a). At the subsequent cycling process, the discharge/charge voltage gradually decreased/increased to 3.03/3.52 V at the 100th cycle, corresponding to 86.1 % efficiency retention (Figures 5b and S23). At 0.10 mA cm^{-2}, the battery exhibited a discharge/charge voltage of 2.92/3.28 V, inducing a round-trip efficiency of 89.0 % at the first cycle (Figure 5c), with a round-trip efficiency of 67.5 % maintained at the 100th cycle (Figure 5d). The theoretical thermodynamic potential of the co-decomposition of Li_2CO_3/C to CO_2/Li^+ is 2.80 V vs. Li^+/Li ($2Li_2CO_3+C \rightarrow 4Li^+ + 4e^- + 3CO_2$, $E^\theta = 2.80$ V vs. Li^+/Li), while the value is 3.82 V vs. Li^+/Li for the self-decomposition of Li_2CO_3 ($2Li_2CO_3 \rightarrow 2CO_2 + O_2 + 4Li^+ + 4e^-$, $E^\theta = 3.82$ V vs. Li^+/Li).[1b] The charge voltages were basically lower than 3.82 V upon cycling in the light, indicating that the charge process were more likely attributed to the co-degradation of Li_2CO_3 and carbon species than the self-decomposition of Li_2CO_3. The decline in efficiency trends upon cycling were reasonably ascribed to the inevitable accumulation of discharge products at the cathode and the volatilization of liquid components in the electrolyte.

In comparison, the batteries in the dark constantly suffered from severe polarized voltages, which would trigger unfavorable decomposition of battery materials and the formation of by-products. Notably, CNT@C_3N_4 heterostructured photocathode achieved lower overpotentials and higher cycling stability than physically-mixed CNT/C_3N_4 and CNT (Figure S24), further confirming the enhanced charge transfer and inhibited carrier recombination at the heterostructure. Besides, the light-assisted Li–CO_2 battery delivered an ultrahigh areal capacity of 15.77 mAh cm^{-2} in CO_2 (Figure S25), revealing superior light-promoted CO_2 reduction kinetics at the heterostructured photocathode. The negligible capacity in argon excluded the intrinsic decompositions of battery materials. Compared with the reported Li–CO_2 batteries, our batteries have demonstrated record-high round-trip efficiency (98.8 %), superior cycling stability at higher areal capacity and current density, and outperformed areal capacity (15.77 mAh cm^{-2}) compared with other counterparts (Figures 5e, f, and Table S1). The batteries also showed a high current tolerance of 1.0 mA cm^{-2} at the rate cycling test (Figure S26). Even at an ultra-low-temperature dry ice bath of around −60 °C, the batteries showed no sharp rise in overpotentials during discharge/charge under illumination (Figure S27), further demonstrating light-promoted CO_2 reduction/evolution processes.

Furthermore, a quasi-solid coaxial Li–CO_2 fiber battery was constructed as a proof-of-concept demonstration (Figure S28). The fiber battery operated efficiently and stably, and powered a blue-light-emitting diode even under intensive bending deformations, suggesting its good flexibility and practicality (Figure S29). Note that the conversion and storage of photo-energy were achieved in this two-electrode flexible device without complex device configuration and circuit connections, which marked an important step towards future self-powered wearable systems.

In conclusion, a CNT@C_3N_4 heterostructured photocathode was designed to promote CO_2 reduction/evolution kinetics of a quasi-solid Li–CO_2 battery under illumination. The unique defective structure of C_3N_4 and favorable charge transfer at heterointerfaces enabled efficient ultraviolet-visible light capture, numerous electron-hole pair generation, and full use of carriers in the target reactions, leading

© 2021 Wiley-VCH GmbH

15213773, 2022, 4, Downloaded from https://onlinelibrary.wiley.com/doi/10.1002/anie.202114612 by Fudan University, Wiley Online Library on [12/12/2024]. See the Terms and Conditions (https://onlinelibrary.wiley.com/terms-and-conditions) on Wiley Online Library for rules of use; OA articles are governed by the applicable Creative Commons License

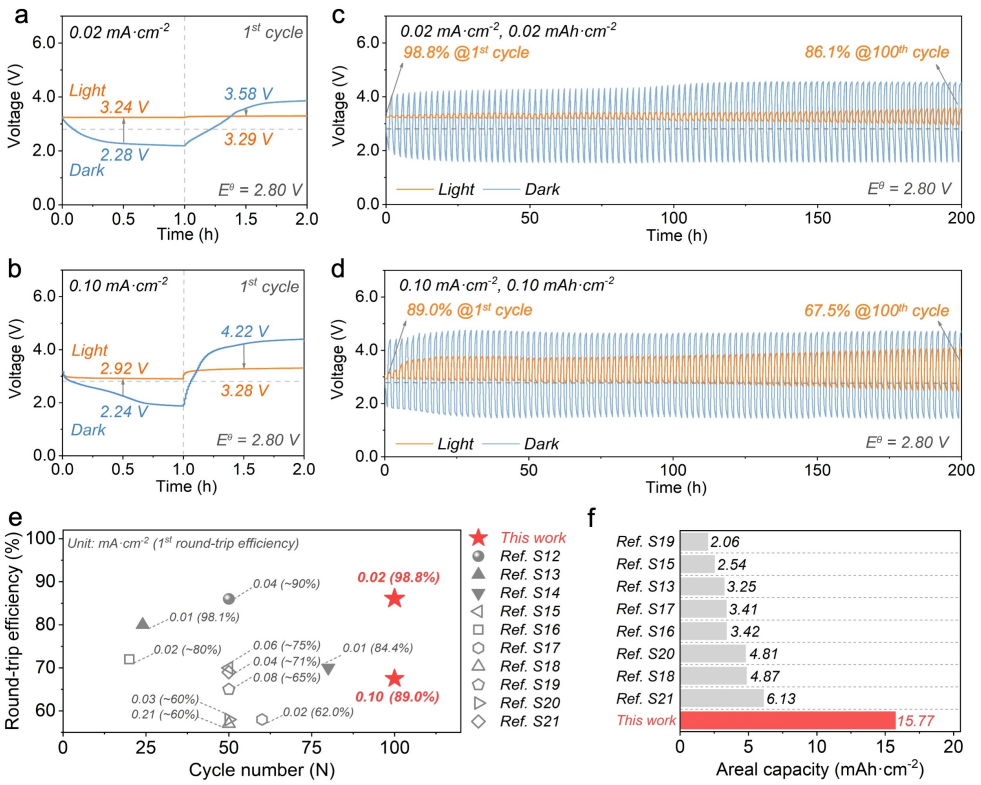

Figure 5. Electrochemical properties of Li–CO_2 batteries based on the CNT@C_3N_4 heterostructured photocathodes. a, b) Discharge/charge curves at the first cycle and c, d) subsequent cycling profiles in the light and dark with current density and cut-off capacity of 0.02/0.10 mA cm^{-2} and 0.02/0.10 mAh cm^{-2}. e, f) Comparison of round-trip efficiencies and areal capacities of Li–CO_2 batteries based on the C_3N_4 heterostructured photocathode and some previously reported excellent Li–CO_2 batteries (involving refs. S12–S21).

to effective photo-energy utilization for decreasing kinetic barriers. Under illumination, photoelectrons rapidly migrate to reduce CO_2 to Li_2CO_3/C during discharge, and holes moved to drive the oxidation of discharge products to CO_2/Li^+ with an applied voltage in the reversible charging process. The resulting Li–CO_2 batteries have achieved high round-trip efficiency of 98.8 % and robust cycling stability with 86.1 % efficiency retention over 100 cycles. The photocathode design provides a general and effective strategy to efficiently utilize photo-energy to address the significant challenges of Li–CO_2 batteries and beyond.

Acknowledgements

The authors sincerely appreciate the help from Zhuo Zhu with the synthesis and characterizations of carbon nitride, Shangyu Li and Wenzhe Niu with the measurement of gas chromatography, Siyu Yan with the measurement of photoluminescence spectroscopy, Yunzhou Wen with the analysis of X-ray photoelectron spectroscopy, and Weijie Zhai with the measurement of the light source. This work was financially supported by MOST (2016YFA0203302), NSFC (21634003), STCSM (20JC1414902), and SHMEC (2017-01-07-00-07-E00062).

Conflict of Interest

The authors declare no conflict of interest.

Data Availability Statement

The data that support the findings of this study are available on request from the corresponding author. The data are not publicly available due to privacy or ethical restrictions.

Keywords: Carbon nanotube · Carbon nitride · Cycling stability · Li–CO_2 battery · Round-trip efficiency

[1] a) B. Liu, Y. Sun, L. Liu, J. Chen, B. Yang, S. Xu, X. Yan, *Energy Environ. Sci.* **2019**, *12*, 887–922; b) Y. Qiao, J. Yi, S. Wu, Y. Qiao, J. Yi, S. Wu, Y. Liu, S. Yang, P. He, H. Zhou, *Joule* **2017**, *1*, 359–370.

[2] a) L. Qie, Y. Lin, J. W. Connell, J. Xu, L. Dai, *Angew. Chem. Int. Ed.* **2017**, *56*, 6970–6974; *Angew. Chem.* **2017**, *129*, 7074–7078; b) J. Li, L. Wang, Y. Zhao, S. Li, X. Fu, B. Wang, H. Peng, *Adv. Funct. Mater.* **2020**, *30*, 2001619.

[3] a) C. Li, Z. Guo, B. Yang, Y. Liu, Y. Wang, Y. Xia, *Angew. Chem. Int. Ed.* **2017**, *56*, 9126–9130; *Angew. Chem.* **2017**, *129*, 9254–9258; b) X. Hu, Z. Li, J. Chen, *Angew. Chem. Int. Ed.* **2017**, *56*, 5785–5789; *Angew. Chem.* **2017**, *129*, 5879–5883; c) C. Hu, L. Gong, Y. Xiao, Z. Xia, L. Ma, T. Wu, Y. Lin, J. Lu, K.

© 2021 Wiley-VCH GmbH

15213773, 2022, 4, Downloaded from https://onlinelibrary.wiley.com/doi/10.1002/anie.202114612 by Fudan University, Wiley Online Library on [12/12/2024]. See the Terms and Conditions (https://onlinelibrary.wiley.com/terms-and-conditions) on Wiley Online Library for rules of use; OA articles are governed by the applicable Creative Commons License

Amine, L. Dai, *Adv. Mater.* **2020**, *32*, 1907436; d) Z. Zhao, E. Wang, J. Wang, C. Liu, Z. Peng, *J. Mater. Chem. A* **2021**, *9*, 3290–3296.

[4] a) K. Baek, W. C. Jeon, S. Woo, J. C. Kim, J. G. Lee, K. An, S. K. Kwak, S. J. Kang, *Nat. Commun.* **2020**, *11*, 456; b) X. Yao, Q. Dong, Q. Cheng, D. Wang, *Angew. Chem. Int. Ed.* **2016**, *55*, 11344–11353; *Angew. Chem.* **2016**, *128*, 11514–11524; c) Z. Tang, Y. Mao, J. Xie, G. Cao, D. Zhuang, G. Zhang, W. Zheng, X. Zhao, *ACS Appl. Mater. Interfaces* **2018**, *10*, 25925–25929.

[5] a) X. Yu, A. Manthiram, *Small Struct.* **2020**, *1*, 2000027; b) Y. Xiao, F. Du, C. Hu, Y. Ding, Z. L. Wang, A. Roy, L. Dai, *ACS Energy Lett.* **2020**, *5*, 916–921; c) Y. Qiao, S. Xu, Y. Liu, J. Dai, H. Xie, Y. Yao, X. Mu, C. Chen, D. J. Kline, E. M. Hitz, B. Liu, J. Song, P. He, M. R. Zachariah, L. Hu, *Energy Environ. Sci.* **2019**, *12*, 1100–1107.

[6] a) N. Yan, X. Gao, *Energy Environ. Mater.* **2021**, https://doi.org/10.1002/eem2.12182; b) Z. Zhu, X. Shi, G. Fan, F. Li, J. Chen, *Angew. Chem. Int. Ed.* **2019**, *58*, 19021–19026; *Angew. Chem.* **2019**, *131*, 19197–19202; c) Y. Liu, N. Li, S. Wu, K. Liao, K. Zhu, J. Yi, H. Zhou, *Energy Environ. Sci.* **2015**, *8*, 2664–2667; d) Q. Lv, Z. Zhu, S. Zhao, L. Wang, Q. Zhao, F. Li, L. A. Archer, J. Chen, *J. Am. Chem. Soc.* **2021**, *143*, 1941–1947; e) C. Zhong, W. Hu, Y. Deng, *Nat. Commun.* **2019**, *10*, 4767; f) M. Li, X. Wang, F. Li, L. Zheng, J. Xu, J. Yu, *Adv. Mater.* **2020**, *32*, 1907098; g) Y. Feng, H. Xue, T. Wang, H. Gong, B. Gao, W. Xia, C. Jiang, J. Li, X. Huang, J. He, *ACS Sustainable Chem. Eng.* **2019**, *7*, 5931–5939; h) H. Gong, H. Xue, B. Gao, Y. Li, X. Fan, S. Zhang, T. Wang, J. He, *Energy Storage Mater.* **2020**, *31*, 11–19.

[7] Z. Zhu, Y. Ni, Q. Lv, J. Geng, W. Xie, F. Li, J. Chen, *Proc. Natl. Acad. Sci. USA* **2021**, *118*, e2024619118.

[8] a) D. Guan, X. Wang, M. Li, F. Li, L. Zheng, X. Huang, J. Xu, *Angew. Chem. Int. Ed.* **2020**, *59*, 19518–19524; *Angew. Chem.* **2020**, *132*, 19686–19692; b) A. Jena, H. Hsieh, S. Thoka, S. Hu, H. Chang, R. Liu, *ChemSusChem* **2020**, *13*, 2719–2725; c) Z. Li, M. Li, X. Wang, D. Guan, W. Liu, J. Xu, *J. Mater. Chem. A* **2020**, *8*, 14799–14806.

[9] a) X. Wang, K. Maeda, A. Thomas, K. Takanabe, G. Xin, J. M. Carlsson, K. Domen, M. Antonietti, *Nat. Mater.* **2009**, *8*, 76–80; b) D. Zhao, C. Dong, B. Wang, C. Chen, Y. Huang, Z. Diao, *Adv. Mater.* **2019**, *31*, 1903545; c) S. Wang, L. Chen, X. Zhao, J. Zhang, Z. Ao, W. Liu, H. Wu, L. Shi, Y. Yin, X. Xu, C. Zhao, X. Duan, S. Wang, H. Sun, *Appl. Catal. B* **2020**, *278*, 119312.

[10] a) L. Chen, R. Yan, M. Oschatz, L. Jiang, M. Antonietti, K. Xiao, *Angew. Chem. Int. Ed.* **2020**, *59*, 9067–9073; *Angew. Chem.* **2020**, *132*, 9152–9158; b) K. Xiao, B. Tu, L. Chen, T. Heil, L. Wen, L. Jiang, M. Antonietti, *Angew. Chem. Int. Ed.* **2019**, *58*, 12574–12579; *Angew. Chem.* **2019**, *131*, 12704–12709.

[11] T. Y. Ma, S. Dai, M. Jaroniec, S. Z. Qiao, *Angew. Chem. Int. Ed.* **2014**, *53*, 7281–7285; *Angew. Chem.* **2014**, *126*, 7409–7413.

[12] E. J. Son, S. H. Lee, S. K. Kuk, M. Pesic, D. S. Choi, J. W. Ko, K. Kim, F. Hollmann, C. B. Park, *Adv. Funct. Mater.* **2018**, *28*, 1705232.

[13] a) A. Du, S. Sanvito, Z. Li, D. Wang, Y. Jiao, T. Liao, Q. Sun, Y. H. Ng, Z. Zhu, R. Amal, S. C. Smith, *J. Am. Chem. Soc.* **2012**, *134*, 4393–4397; b) X. Li, Y. Dai, Y. Ma, S. Han, B. Huang, *Phys. Chem. Chem. Phys.* **2014**, *16*, 4230–4235; c) X. Han, J. Chen, M. Chen, W. Zhou, X. Zhou, G. Wang, C. P. Wong, B. Liu, L. Luo, S. Chen, S. Shi, *Energy Storage Mater.* **2021**, *39*, 250–258.

[14] K. Awazu, M. Fujimaki, C. Rockstuhl, J. Tominaga, H. Murakami, Y. Ohki, N. Yoshida, T. Watanabe, *J. Am. Chem. Soc.* **2008**, *130*, 1676–1680.

[15] a) N. B. Aetukuri, B. D. McCloskey, J. M. Garciá, L. E. Krupp, V. Viswanathan, A. C. Luntz, *Nat. Chem.* **2015**, *7*, 50–56; b) J. Chen, K. Zou, P. Ding, J. Deng, C. Zha, Y. Hu, X. Zhao, *Adv. Mater.* **2019**, *31*, 1805484.

[16] Y. Qiao, S. Wu, J. Yi, Y. Sun, S. Guo, S. Yang, P. He, H. Zhou, *Angew. Chem. Int. Ed.* **2017**, *56*, 4960–4964; *Angew. Chem.* **2017**, *129*, 5042–5046.

[17] P. Wang, Y. Ren, R. Wang, P. Zhang, M. Ding, C. Li, D. Zhao, Z. Qian, Z. Zhang, L. Zhang, L. Yin, *Nat. Commun.* **2020**, *11*, 1576.

[18] Y. Xing, Y. Yang, D. Li, M. Luo, N. Chen, Y. Ye, J. Qian, L. Li, D. Yang, F. Wu, S. Guo, *Adv. Mater.* **2018**, *30*, 1803124.

[19] a) Y. Qiao, Y. Liu, K. Jiang, X. Li, Y. He, Q. Li, S. Wu, H. Zhou, *Small Methods* **2018**, *2*, 1700284; b) C. Tang, P. Sun, J. Xie, Z. Tang, Z. Yang, Z. Dong, *Energy Storage Mater.* **2017**, *9*, 206–213.

Manuscript received: October 28, 2021
Accepted manuscript online: November 19, 2021
Version of record online: December 7, 2021

© 2021 Wiley-VCH GmbH

15213773, 2022, 4, Downloaded from https://onlinelibrary.wiley.com/doi/10.1002/anie.202114612 by Fudan University, Wiley Online Library on [12/12/2024]. See the Terms and Conditions (https://onlinelibrary.wiley.com/terms-and-conditions) on Wiley Online Library for rules of use; OA articles are governed by the applicable Creative Commons License